Engineering Fracture Mechanics 202 (2018) 487–499

Contents lists available at ScienceDirect

Engineering Fracture Mechanics

journal homepage: www.elsevier.com/locate/engfracmech

Determination of interface toughness of functionally graded tungsten/EUROFER multilayer at 550 °C by analytical and experimental methods

D. Qu[a,b,*], E. Gaganidze[a], R. Vaßen[c], J. Aktaa[a]

[a] Karlsruhe Institute of Technology, Institute for Applied Materials, Hermann-von-Helmholtz-Platz 1, 76344 Eggenstein-Leopoldshafen, Germany
[b] Institute of Mechanics, Chinese Academy of Sciences, Beijing 100190, China
[c] Forschungszentrum Jülich, Institute of Energy and Climate Research (IEK-1), Jülich, Germany

ARTICLE INFO

Keywords:
FG tungsten/EUROFER multilayer
Interface toughness
Bending test
Energy release rate

ABSTRACT

As armor coating, functionally graded (FG) tungsten/EUROFER multilayer was sprayed on EUROFER substrate for First Wall application in fusion field. Interface toughness between FG tungsten/EUROFER multilayer and EUROFER substrate was studied innovatively by a simple method based on the beam theory in this paper. To quantify interface toughness, the energy release rate was assessed by performing three and four-point bending tests on pre-cracked specimens at 550 °C and under high vacuum. The energy release rate during propagating of interfacial crack was determined to be 258 J/m^2 and 225 J/m^2 analytically and experimentally for samples with 3 and 5 layers as FG-layer, respectively, which were calculated based on multi bending tests. Cross-section and fracture microstructure show a vast of plasticity in FG-layer, particularly in FG-layer with a higher volume ratio of EUROFER. Interfacial fracture microstructure indicates interface adhesion consists of mechanical interlocking and metallurgical bonding.

1. Introduction

Tungsten coating is considered as armor material for first wall (FW) in the current European DEMO blanket concepts [1], primarily due to its high melting point, low sputtering yield, high thermal conductivity and low activation [2,3]. For overcoming the large mismatch in thermo-physical properties between tungsten coating and reduced activation ferritic/martensitic (RAFM) steels, e.g. EUROFER as the FW material [4], functionally graded material (FGM) has been introduced to reduce the residual stress [5]. EUROFER developed recently interalia in the framework of EURATOM Fusion Technology programme, is a potential candidate for structural materials of future fusion reactors [6]. The chemical composition of EUROFER are Cr 8.93, C 0.12, Mn 0.47, V 0.2, W 1.07, Ta 0.14, N_2 0.018, and Fe balance (wt%) [7]. The potential of the FGM in reducing inelastic strains and improving lifetime was demonstrated [8], and the investigated thickness of FG-layer was suggested by non-linear finite element (FE) simulation [5]. Based on the results of simulation, tungsten coating with FG tungsten/EUROFER layer on EUROFER substrate (FG tungsten/EUROFER

Abbreviations: FG(M), functionally graded (material); FW, first wall; DEMO, demonstration fusion reactor; RAFM, reduced activation ferritic/martensitic; VPS, vacuum plasma spraying; FE, finite element; CTOD, crack-tip-opening displacement; SEM, scanning electron microscope; EDX, energy dispersive X-ray spectroscopy; EDM, electrical discharge machining

* Corresponding author at: Institute of Mechanics, Chinese Academy of Sciences, Beijing 100190, China.
E-mail address: dandanqu@imech.ac.cn (D. Qu).

https://doi.org/10.1016/j.engfracmech.2018.09.016
Received 21 January 2018; Received in revised form 3 September 2018; Accepted 7 September 2018
Available online 13 September 2018
0013-7944/

Nomenclature

Σ_{sub}	stiffness of substrate	$\vartheta_{W50\%}$	Poisson's ratio of coating with 50% tungsten
Σ_c	stiffness of composite	$\vartheta_{W37\%}$	Poisson's ratio of coating with 37% tungsten
I_c	moment of inertia for the composite	$\vartheta_{W25\%}$	Poisson's ratio of coating with 25% tungsten
E_W	Young's modulus of tungsten coating	ϑ_1	Poisson's ratio of multilayer
$E_{W75\%}$	Young's modulus of coating with 75% tungsten	ϑ_2	Poisson's ratio of substrate
$E_{W63\%}$	Young's modulus of coating with 63% tungsten	B	width of composite beam
$E_{W50\%}$	Young's modulus of coating with 50% tungsten	h	thickness of composite beam
$E_{W37\%}$	Young's modulus of coating with 37% tungsten	h_1	thickness of multilayer
$E_{W25\%}$	Young's modulus of coating with 25% tungsten	h_2	thickness of substrate
E_1	Young's modulus of multilayer	λ	material parameter
E_c	Young's modulus of composite beam	T_W	thickness of tungsten coating
ϑ_W	Poisson's ratio of tungsten coating	$T_{W75\%}$	thickness of coating with 75% tungsten
$\vartheta_{W75\%}$	Poisson's ratio of coating with 75% tungsten	$T_{W63\%}$	thickness of coating with 63% tungsten
$\vartheta_{W63\%}$	Poisson's ratio of coating with 63% tungsten	$T_{W50\%}$	thickness of coating with 50% tungsten
		$T_{W37\%}$	thickness of coating with 37% tungsten
		$T_{W25\%}$	thickness of coating with 25% tungsten

multilayer) was fabricated by vacuum plasma spraying (VPS) [9]. VPS was chosen for fabricating FG tungsten/EUROFER multilayer owing to the ability to achieve a full range of graded chemical composition, in-situ repairing as well as the avoidance of oxide formation [8,10,11] and a large area with a relatively high coating rate [12]. The FG tungsten/EUROFER multilayers produced in this project have expected nominal microstructure with pancake-like features, columnar grains as well as low porosity and sound almost seamless interfaces between the FG-layer and the EUROFER substrate [9]. There are lately several theories on static bending and buckling of FG plates, including a non-classical Kirchhoff plate theory [13], a non-classical simple first-order shear deformation theory [14], Kirchhoff-Love theory [15] and a new simple third order shear deformation plate theory [16]. In addition to FGM with in-plane material inhomogeneity studied in Ref. [15], FGM with material inhomogeneity along the thickness direction are investigated in the project.

Interface toughness is a critical assessment of the thermal spray coating quality and the interfacial adhesion strength since fracture at interfaces is a very common and a critical phenomenon in many systems, for example, laminar composites, microelectronic devices and thin films. Irwin [17] developed the energy release rate concept in 1956. It was derived from the Griffith theory but was more useful for solving engineering problems. Around 1960, researchers turned their attention to crack-tip plasticity when the fundamentals of linear elastic fracture mechanics were fairly well established. Besides the crack-tip-opening displacement (CTOD) proposed by Wells, Rice developed J-integral to characterize nonlinear material behavior ahead of a crack [18]. A series of methods on determining interface toughness/interface debonding strength were established based on the above theory. The researches include: three-point and four-point bending test on a laminated SiC/C composite [19], three-point bending test on a $Si_3N_4/BN(Al_2O_3)/Si_3N_4$ sandwiched sample [20], and four-point bending test on AI/PMMA bonded sample [21] and plasma sprayed B_4C coating on Ti-6AI-4V substrate [22]. Besides three-point and four-point bending test methods, double cantilever beam [23] and indentation method [24,25] were also widely used for measuring the interface toughness.

In this work, material properties including Young's modulus and Poisson's ratio of FG tungsten/EUROFER multilayer and the stiffness of the composite were determined first, afterwards the formula for calculating the interface toughness was analytically deduced based on the beam theory. Three- and four-point bending tests on pre-cracked specimens were performed for the determination of the interface toughness. The fracture microstructures in the FG-layer and on the interface were analyzed by SEM and EDX.

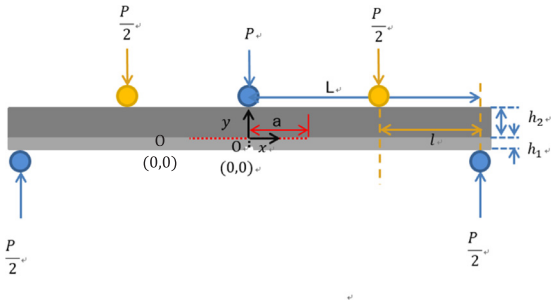

Fig. 1. Schematic view of the beam for 3 (blue balls) and 4 point (two yellow balls and two blue balls) bending test. (For interpretation of the references to colour in this figure legend, the reader is referred to the web version of this article.)

2. Analytical method and experiment

2.1. Analytical method

Three and four-point bending tests were carried out to evaluate the interface toughness of FG W/EUROFER multilayer since the beam bending theory is simple and effective. A schematic view of the beam for bending tests is shown in Fig. 1. The pre-crack and the through-thickness cracks are assumed to occur in the center of the beam and the interfacial cracks propagate symmetrically from the center. Based on the beam theory and plane strain condition, the estimated value of the steady-state energy release rate can be obtained analytically. Specifically, the expression of the roller displacement can be established first, and then the expression of compliance can be obtained since it is equal to the displacement divided by the load. In the end, we got the expression of strain energy release rate by differentiating the expression of compliance [26].

For calculating the interface toughness, the Young's modulus, Poisson's ratio and stiffness of the composite beam need to be primarily determined. According to the definition of the moment of inertia and stiffness, the stiffness of the substrate, Σ_{sub}, can be calculated based on the formula (1). The moment of inertia of the composite was developed by Charalambides et al. [21] and showed in the formula (2) by introducing the formula (7), a function of the Young's moduli and Poisson's ratios of constituting materials. Based on the definition of stiffness, the stiffness of the composite can be determined according to the formula (4) combined with the formula (3) and the formula (2). In addition, the Young's modulus and the Poisson's ratio of the multilayer were interpolated from those of the bulk material assuming the proportion of each layer to be related to their thickness, as shown in the formula (5) and the formula (6).

$$\Sigma_{sub} = \frac{Bh_2^3}{12} \times E_{sub} \tag{1}$$

$$I_c = \frac{h_1^3}{12} + \frac{\lambda h_2^3}{12} + \frac{\lambda h_1 h_2 (h_1 + h_2)^2}{4(h_1 + \lambda h_2)} \quad [21] \tag{2}$$

$$E_c = \frac{E_1 \times h_1 + E_2 \times h_2}{h} \tag{3}$$

$$\Sigma_c = I_c \times B \times E_c \tag{4}$$

where

$$E_1 = \frac{E_w \times T_w + E_{w75\%} \times T_{w75\%} + E_{w63\%} \times T_{w63\%} + E_{w50\%} \times T_{w50\%} + E_{w37\%} \times T_{w37\%} + E_{w25\%} \times T_{w25\%}}{T_w + T_{w75\%} + T_{w63\%} + T_{w50\%} + T_{w37\%} + T_{w25\%}} \tag{5}$$

$$\vartheta_1 = \frac{\vartheta_w \times T_w + \vartheta_{w75\%} \times T_{w75\%} + \vartheta_{w63\%} \times T_{w63\%} + \vartheta_{w50\%} \times T_{w50\%} + \vartheta_{w37\%} \times T_{w37\%} + \vartheta_{w25\%} \times T_{w25\%}}{T_w + T_{w75\%} + T_{w63\%} + T_{w50\%} + T_{w37\%} + T_{w25\%}} \tag{6}$$

$$\lambda = \frac{E_2(1-\vartheta_1^2)}{E_1(1-\vartheta_2^2)} \quad [21] \tag{7}$$

$$h = h_1 + h_2 \tag{8}$$

E_1, E_2 and $E_c$are the Young's modulus of the multilayer, the substrate and the composite specimen, respectively. ϑ_1 and ϑ_2 are the Poisson's ratios of the multilayer and the substrate. The material parameter λ is an expression of the Young's modulus and Poisson's ratio of both materials. B and$h$ are the width and the thickness of the specimen. $h_1$and h_2 are the thicknesses of the multilayer and the substrate, respectively. Σ_{sub} and $\Sigma_c$are the stiffness of the substrate and the whole composite specimen. I_c is the moment of inertia per unit width for the composite.

2.1.1. 3-P bending test

The interfacial crack propagation in the composite specimen can be segregated into two stages. The first stage is the interfacial cracking. With bending goes on, interfacial crack propagation is replaced by general plastic deformation of the substrate, which is the second stage. The composite is assumed to carry the stress in the first stage. Therefore, the beam stiffness in the first stage is the composite stiffness. For the second stage, only the substrate is supposed to carry the applied stress, so the beam stiffness is equal to the substrate stiffness.

According to the beam theory, during the first stage, the deflections of the specimen can be evaluated by the following formula assuming that the composite specimen carries the stress:

$$\frac{d^2y_1}{dx^2} = -\frac{Px}{2\Sigma_c} \tag{9}$$

For the second stage, only the substrate is supposed to carry the stress:

$$\frac{d^2y_2}{dx^2} = -\frac{Px}{2\Sigma_{sub}} \tag{10}$$

where y_1 and y_2 are the deflection of the neutral axis during the first and second stage, respectively. And Σ_c and Σ_{sub} are the stiffness of the composite specimen and the substrate, respectively.

The mathematical relation between the deflection of the central loading point and the propagating crack length a can be obtained based on the following boundary conditions of the model.

For $x \in (0, L-a)$

$$\frac{d^2y_1}{dx^2} = -\frac{Px}{2\Sigma_c} \tag{11}$$

For $x \in (L-a, L)$

$$\frac{d^2y_2}{dx^2} = -\frac{Px}{2\Sigma_{sub}} \tag{12}$$

The boundary conditions:

$$y_{1|x=0} = 0 \tag{13}$$

$$\frac{dy_1}{dx}_{|x=(L-a)} = \frac{dy_2}{dx}_{|x=(L-a)} \tag{14}$$

$$y_{1|x=(L-a)} = y_{2|x=(L-a)} \tag{15}$$

$$\frac{dy_2}{dx}_{|x=L} = 0 \tag{16}$$

The derivational process and the boundary conditions are specified as following:

After the first integration,

$$\frac{dy_1}{dx} = -\frac{Px^2}{4\Sigma_c} + A_1 \tag{17}$$

$$\frac{dy_2}{dx} = -\frac{Px^2}{4\Sigma_{sub}} + B_1 \tag{18}$$

After the second integration,

$$y_1 = -\frac{Px^3}{12\Sigma_c} + A_1x + A_2 \tag{19}$$

$$y_2 = -\frac{Px^3}{12\Sigma_{sub}} + B_1x + B_2 \tag{20}$$

where A_1, A_2, B_1 and B_2 are constant values.

When substituting the boundary conditions, the constant values are obtained:

$$A_2 = 0 \tag{21}$$

$$A_1 = \frac{P(L-a)^2}{4\Sigma_c} - \frac{P(L-a)^2}{4\Sigma_{sub}} + \frac{PL^2}{4\Sigma_{sub}} \tag{22}$$

$$B_1 = \frac{PL^2}{4\Sigma_{sub}} \tag{23}$$

$$B_2 = \frac{P(L-a)^3}{6}\left(\frac{1}{\Sigma_c} - \frac{1}{\Sigma_{sub}}\right) \tag{24}$$

Then the deflection at the central point can be expressed:

$$y = \frac{PL^3}{6\Sigma_{sub}} + \frac{P(L-a)^3}{6}\left(\frac{1}{\Sigma_c} - \frac{1}{\Sigma_{sub}}\right) \tag{25}$$

Since the compliance $= \frac{y}{P}$, then

$$C = \frac{L^3}{6\Sigma_{sub}} + \frac{1}{6}\left(\frac{1}{\Sigma_c} - \frac{1}{\Sigma_{sub}}\right)(L-a)^3 \tag{26}$$

If we assume the propagating cracks are symmetric on both sides of the central point, the interface toughness can be obtained according to the fracture mechanic expression:

$$G_c = \frac{P^2}{4B}\frac{dC}{da} \tag{27}$$

After the differentiation of the formula (26), the interface toughness can be expressed as:

$$G_c = -\frac{P^2}{8B}\left(\frac{1}{\Sigma_c}-\frac{1}{\Sigma_{sub}}\right)(L-a)^2 \tag{28}$$

2.1.2. 4-P bending based on charalambides's model

The specimen was subjected to a constant moment condition when the crack located between the inner loading lines during four-point bending test. Therefore, the strain energy release rate should exhibit steady-state characteristics. The steady-state value, G_{ss}, has been deduced analytically by recognizing that it is simply the difference in strain energy in the uncracked and cracked beam. Then the strain energy release rate can be expressed by the formula (29), which is deduced from Euler-Bernoulli beam theory and plane strain conditions [21]. As shown in Fig. 2, the steady-state value G_{ss} increases with the thickness ratio, and it decreases with the

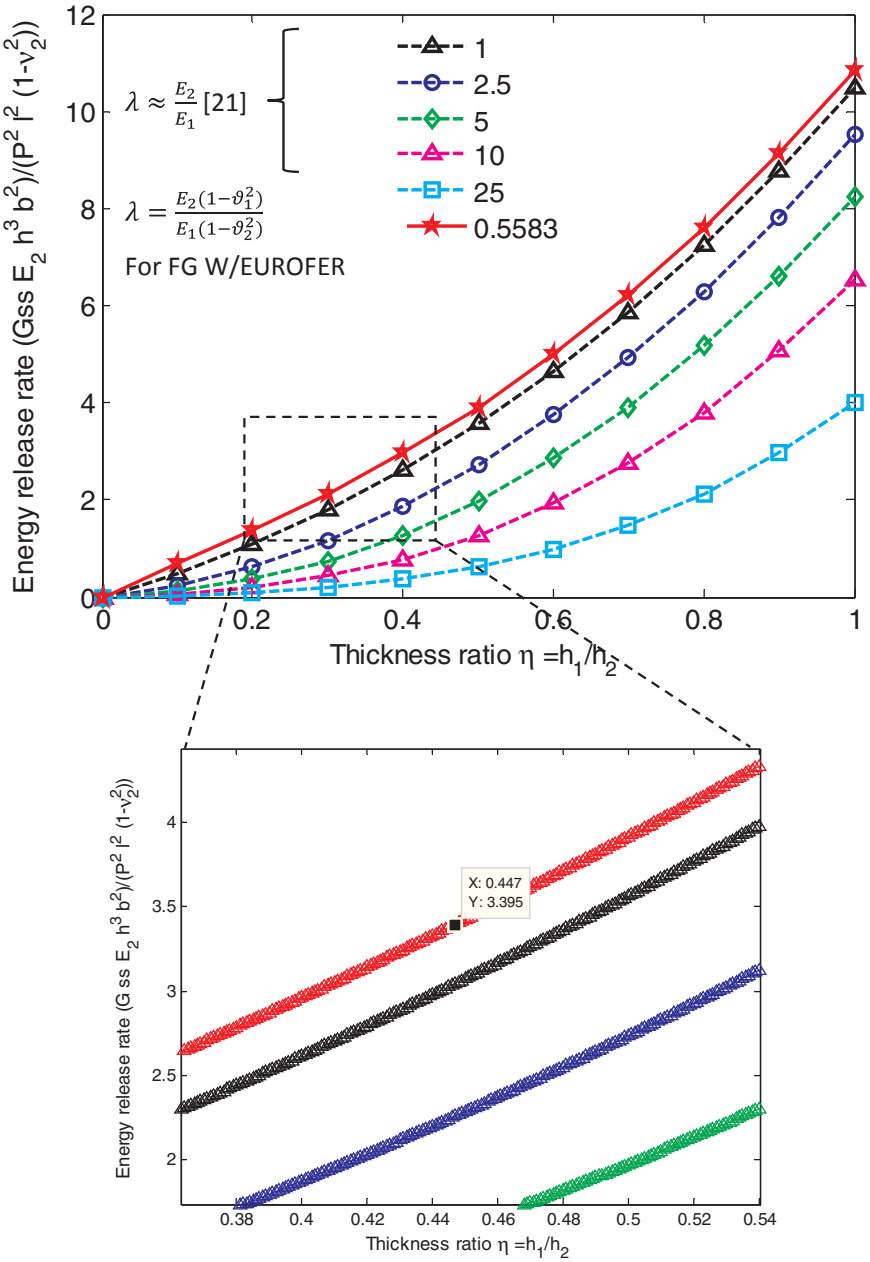

Fig. 2. The steady-state energy release rate vs. the thickness ratio and material parameter λ from Ref. [21] (dotted lines) and FG W/EUROFER multilayer (solid line).

material parameter λ. The dotted lines and the markers are the analytical and finite element results by Charalambides et al. [21], respectively. As it can be seen, the two results fit very well, what proves the analytical model reliability. Applying the model to FG W/EUROFER multilayer, the energy release rate as a function of the thickness ratio is plotted in Fig. 2 for one sample with the certain λ. Four-point bending tests were performed to determine the critical load during the propagation of the interfacial crack,

$$\frac{E_2 G_{ss} h^3 B^2}{P^2 l^2 (1-\vartheta_2^2)} = \frac{3}{2}\left\{\frac{1}{\left(\frac{h_2}{h}\right)^3} - \frac{\lambda}{\left(\frac{h_1}{h}\right)^3 + \lambda\left(\frac{h_2}{h}\right)^3 + 3\lambda\left(\frac{h_1 h_2}{h^2}\right)\left(\frac{h_1}{h} + \frac{\lambda h_2}{h}\right)^{-1}}\right\} \tag{29}$$

where $G_{ss}$is the steady-state energy release rate, P is the load of the propagation of the interfacial crack, l is the distance between inner and outer load lines.

2.2. Specimen and Set-up

Five multilayers with the same top tungsten coating and different FG-layer (variable thicknesses and layer numbers) were deposited on EUROFER substrates by VPS. Both tungsten and EUROFER powders were sprayed synchronously from two nozzles, melted and mixed before they solidified on the substrate.

Five samples were named n-T(i) according to the layer number n and the nominal thickness i in 100 μm of FG-layer. Three and five stepwise layers were introduced to represent linear gradient considering the feasibility of the fabrication process. The volume concentration of tungsten in the FG-layer gradually increased from the substrate to the tungsten coating. The true concentrations of tungsten were introduced in Ref. [9], the true concentration of tungsten followed a globally linear gradient. Samples with five layers showed a smoother gradient than those with three layers.

The thickness of the top tungsten coating was designed to be 500 μm for all the samples, while the nominal thicknesses of FG-layer were designed to be 300, 500 and 700 μm according to the simulation results [5]. The same nominal thickness was specified for 3-T(5) and 5-T(5), as well as for 3-T(7) and 5-T(7). However, the true thicknesses of the FG-layer and the whole multilayer were a bit larger than the nominal ones, in particular, the true thicknesses of 3-T(7) and 5-T(7) were 1322 and 1443 μm, respectively [9,27].

Samples 5-T(7), 3-T(5) and 3-T(7) were cut into specimens with the dimension of 27 x 4 x 3 mm^3 (L × W × B) for three-point bending. In the case of four-point bending test, sample 3-T(7) was machined into specimens with the dimension of 45 x 4 x 3 mm^3 (L × W × B). In both kinds of specimens, 0.5 mm deep notch was cut by electrical discharge machining (EDM). Two lateral surfaces of the specimen were ground and polished for observing the crack. A through-thickness fatigue pre-crack was introduced by resonating fatigue machine. The length of pre-crack was in the range of 140 − 820 μm, whereas all pre-cracks tips were inside the FG-layer.

Lengths of the notch and pre-crack, as well as width and thickness of each specimen were measured before bending tests. For the cases that the lengths of pre-cracks on both sides were not uniform, the mean value was taken for the calculation. For the cases that the pre-crack was only observed on one side, the calculated value was considered to be invalid. According to the non-linear FE-simulation considering the design of the European helium cooled pebble bed Test Blanket Module as reference, the operation temperature of FW is 550 °C [28]. The three-point and four-point bending tests were performed at 550 °C in a vacuum furnace, and the set-ups are shown in

Fig. 3. It is necessary to calibrate the temperature to achieve a stable temperature field at 550 °C during the bending test. The deflection was measured and controlled by a transducer.

Fig. 4 shows the schematic of load and moment of three-point (a) and four-point (b) bending tests. Comparing to three-point bending, four-point bending has the advantage that it can provide a constant moment between the two inner loading points. In this paper, three-point bending tests were performed firstly to obtain experimental data including pre-crack preparation methods since

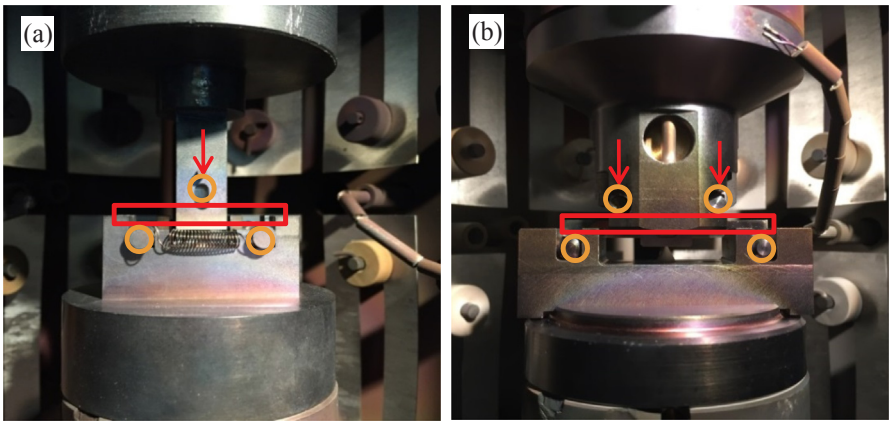

Fig. 3. Set-ups: (a) three-point bending and (b) four-point bending.

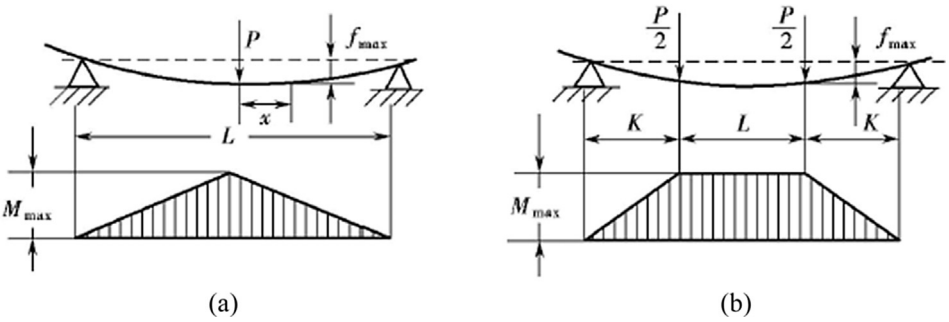

Fig. 4. Schematic view of load and moment for three-point (a) and four-point (b) bending.

the limited samples' dimension and samples of larger size are required for four-point bending test. Meanwhile, mechanical strength measured by four-point bending should be lower and much reliable than the one measured by three-point bending.

3. Results and discussion

3.1. Load-displacement curve

Fig. 5(a) shows load vs. deflection curves during three-point bending tests of the samples 3-T(5), 3-T(7) and 5-T(7). Two tests on specimens of 5-T(7) (black and red lines of Fig. 5(a)) were performed with a relatively large loading and unloading rate (0.5 μm/s), while the rate for the other tests was kept equal to 0.2 μm/s for obtaining more details during loading. Obviously the geometry effect is observed due to the influence of plate stiffness. Samples 3-T(7) and 5-T(7) have more or less the same thicknesses of FG-layer and substrates, therefore, the bearing part during the bending test is more or less the same that leads to comparable maximum loads. While the thinner FG-layer of samples 3-T(5) and accordingly thicker bearing substrate results in the largest bending load. Fig. 5(b) shows load vs. deflection curves of the sample 3-T(7) measured during four-point bending tests.

As it can be seen from Fig. 5(a) and (b), after the monotonic elasto-plastic increase of the loads, loads drop down from the peak

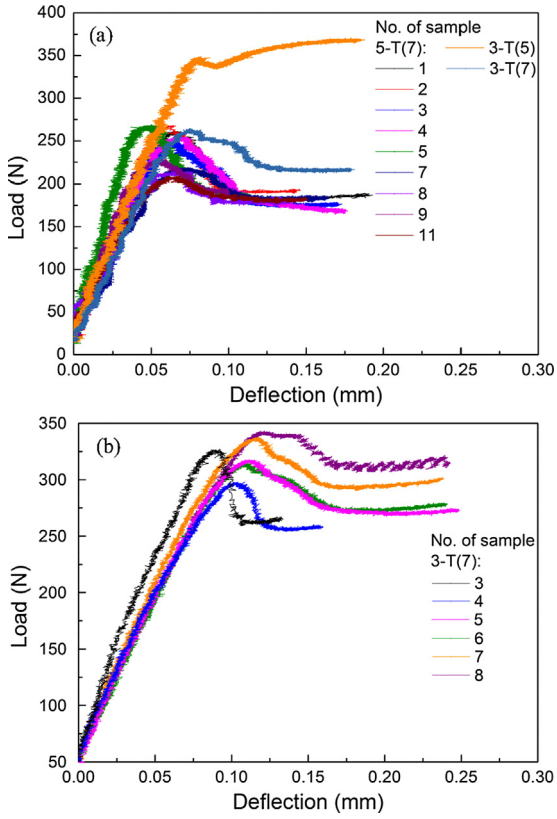

Fig. 5. Load vs. deflection curves of pre-cracked specimens during three-point (a) and four-point (b) bending tests.

and then keep constant for all specimens. For better understanding, a CCD camera was installed outside the furnace to monitor the specimen. Thereby plastic deformation was observed at the tip of the pre-crack. Drops of load were a direct result of the propagation of the crack as well as additional secondary cracks in the FG-layer. The load keeps falling until it becomes constant where the main crack deflects along the FG-layer/substrate interface.

Load gradually drops at one, two, or three stages with a nearly constant rate in each stage. Comparing the position of the pre-crack tip of each specimen, the cases with more than one dropping rate occurred mostly in specimens that the pre-crack tip was in the FG-layer with the concentration of tungsten lower than 50%. The reason is that the FG-layer with the concentration of tungsten lower than 50% behaves more ductile, and therefore the energy required for crack propagation is higher. The propagation of the crack in FG-layer is not always perpendicular straight to the FG-layer/substrate interface, but accompanied by propagations into small interfaces among the laminar layers with possibly weak bonding strength. This zigzag crack is proven by the video of crack propagation and the optical microstructure of specimen after bending, as shown in Fig. 6. Nevertheless, all main cracks propagate through the entire multilayer and deflect along the FG-layer/substrate interface, and propagate a certain distance along this interface.

3.2. Microstructure of crack in FG-layer and on the interface

Fig. 7 shows the crack propagation on the cross-section of sample 5-T(7) after three-point bending tests. A throughout crack propagates in the whole FG-layer, and then deflects along the FG-layer/substrate interface, as illustrated in Fig. 7(a) and (b). Details of crack propagation in FG-layer are presented in Fig. 7(c). Comparing to the brittle fracture characteristic in W75% (nominal concentration in vol.%) layer of FG-layer, crooked shape and plastic fracture characteristics have been observed in the others FG layers. In Fig. 7 a ductile deformation area is marked by the red ellipse and delaminations are pointed out by arrows among laminar interfaces in FG-layer. These delaminations consume energy during the crack propagation and hence hinder further propagation of the crack in the main failure direction.

The fracture microstructure inside the FG-layer is observed and presented in Fig. 8. As it can be seen, the fracture surfaces are rough and uneven. The delamination among laminar interfaces showed in the cross-section microstructure is much clearly observed in Fig. 8(a). In addition, there are a vast amount of plastic deformation in the FG-layer with the concentration of W25% (e.g. dimples in Fig. 8(b)) and intergranular fracture in the FG-layer with the concentration of W75% that is the main fracture mechanism of W in Fig. 8(c).

The specimens after bending tests were oxidized at 300 °C for 2 h, and then were broken instantaneously after sinking into liquid nitrogen to observe the fracture microstructure. Due to the oxidation of fracture surface introduced by bending, the fracture microstructure can be separated into two parts by the red line shown in Fig. 9(a). As shown in Fig. 9(b), the ductile fracture characteristic is observed at the coating-side of the interface. Both brittle and ductile fracture characteristics are observed at the substrate-side interface, as shown in Fig. 9(c) and (d). There were few cleavage type fractures due to the mechanical interlocking. Nevertheless, many micropores were formed in the initial state of ductile fracture, which indicating the metallurgic bonding on the interface.

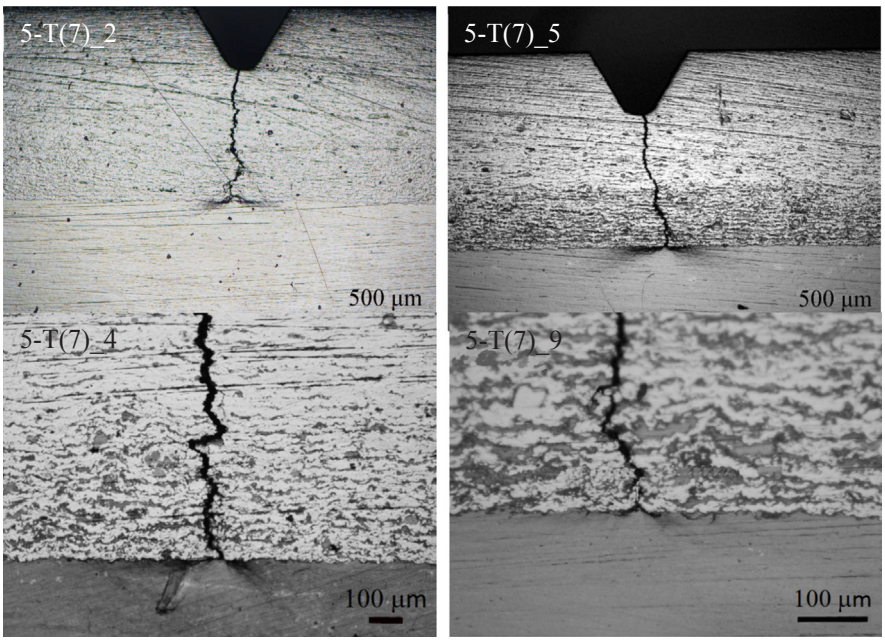

Fig. 6. Optical microstructure of pre-cracked specimens after three-point bending.

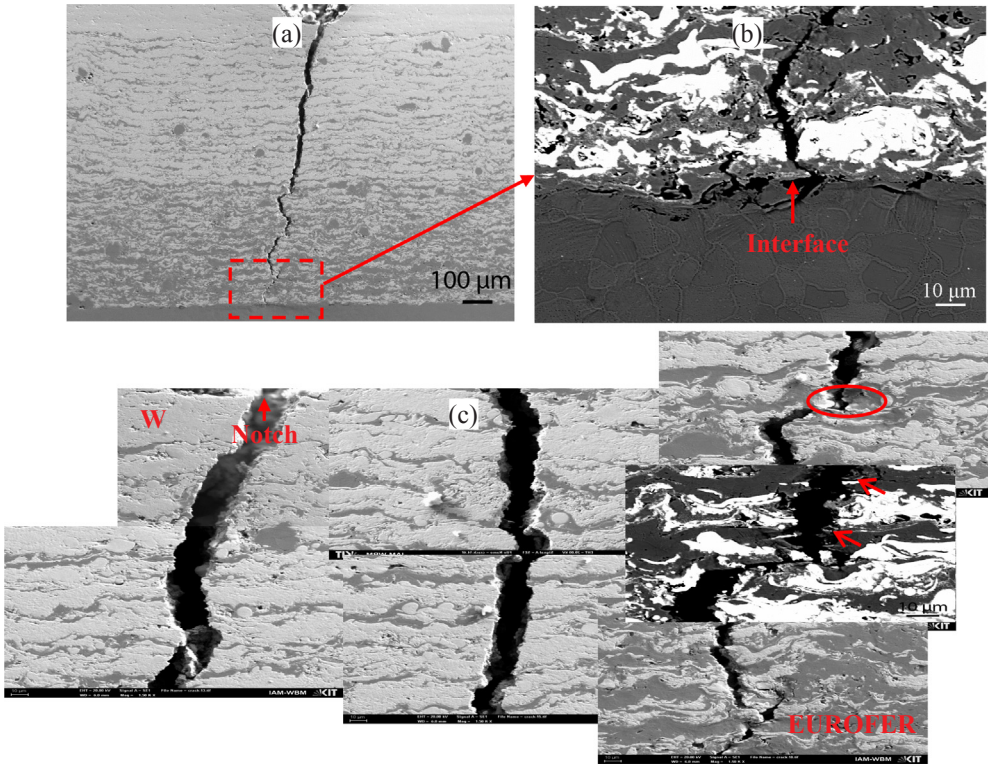

Fig. 7. The crack propagation within FG-layer (a, c) and along the substrate interface (b) on the cross-section of sample 5-T(7) after three-point bending.

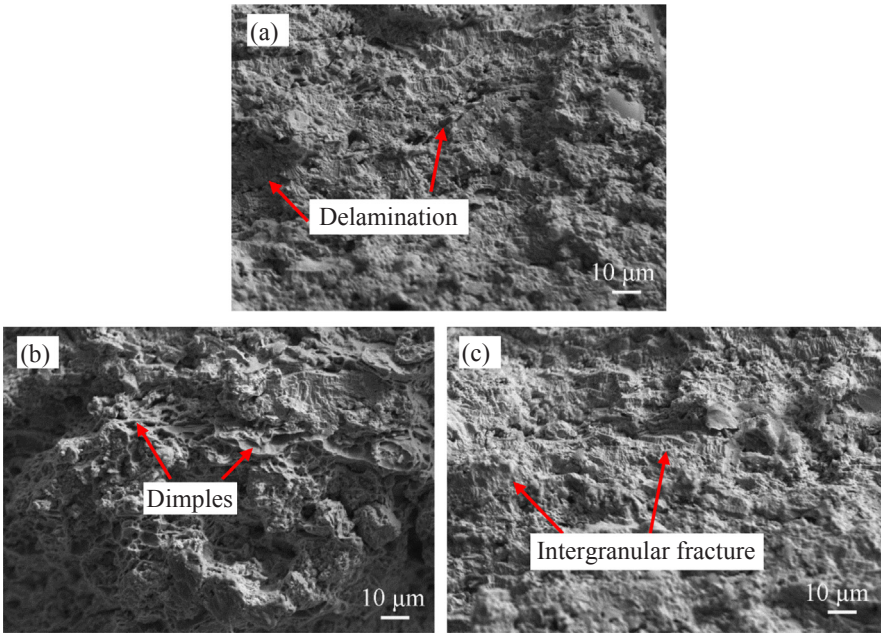

Fig. 8. Fracture surface within the FG-layer with the nominal concentration of W(vol.%): (a) 50%; (b) 25%; (c) 75%.

3.3. Interface toughness

Interface toughness of FG W/EUROFER multilayers with the same nominal thickness of FG-layer and two kinds of layer numbers determined by three- and four-point bending tests, respectively are indicated in Tables 1. In addition, Tables 1 show the measured

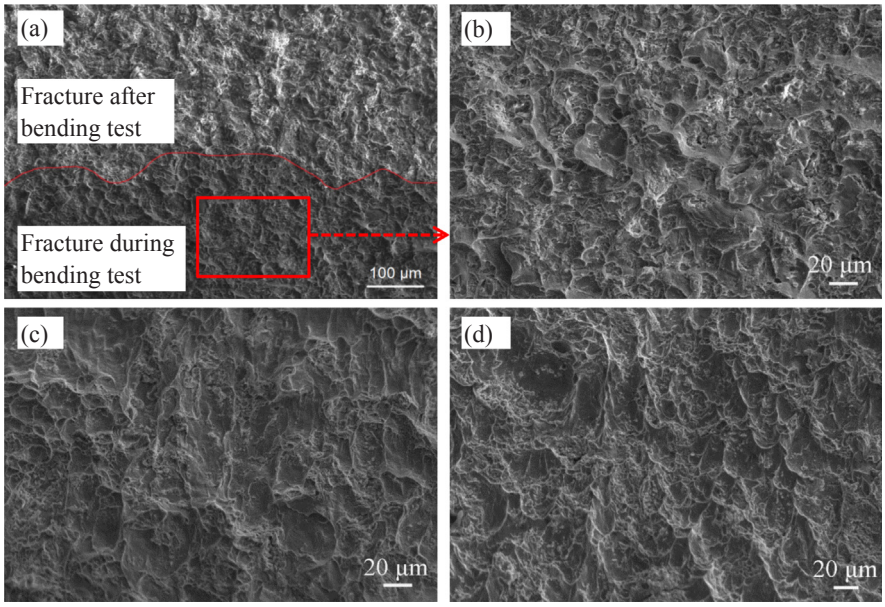

Fig. 9. Fracture microstructure on the interface: (a) and (b) coating-side; (c) and (d) substrate-side interface.

Table 1a
Interface toughness of sample 3-T(7) calculated based on three-point bending tests.

Symbol of specimen	87-2	87-3	87-4	87-6	87-7	87-8	New 87-1
h_1 (mm)	1.27	1.26	1.25	1.27	1.28	1.28	1.26
h (mm)	3.94	3.93	3.91	3.92	3.91	3.92	3.94
B (mm)	3.01	3.01	3.01	2.98	2.99	3	3.01
P_c(N)	197.59	205.14	171.43	188.51	186.97	205.56	221.14
a_c (10^{-3} m)	0.49	0.33	0.26	0.27	0.13	0.28	0.28
G_c(J/m^2)	252.30	277.61	194.65	240.80	239.65	282.19	326.08

Table 1b
Interface toughness of sample 5-T(7) calculated based on three-point bending tests.

Symbol of specimen	103-2	103-3	103-4	103-5	103-7	103-8	103-9	103-11
h_1 (mm)	1.42	1.38	1.41	1.40	1.40	1.39	1.39	1.40
h (mm)	3.96	3.96	3.95	3.95	3.96	3.97	3.97	3.96
B (mm)	3.01	3	2.98	2.98	2.96	2.96	2.97	2.97
P_c(N)	191.35	176.44	173.67	189.58	183.42	179.42	191.05	181.27
a_c (10^{-3} m)	0.21	0.05	0.56	0.14	0.21	0.08	0.04	0.29
G_c(J/m^2)	239.32	209.26	190.04	241.24	227.38	222.39	251.98	217.71

Table 2
Interface toughness of sample 3-T(7) calculated based on four-point bending tests.

Symbol of specimen	87-3	87-4	87-5	87-6	87-7	87-8
B (mm)	2.93	2.94	2.95	2.98	2.95	2.92
h (mm)	3.87	3.86	3.9	3.88	3.92	3.90
h_1 (mm)	1.22	1.19	1.20	1.19	1.21	1.18
h_1/h_2	0.463	0.447	0.445	0.442	0.447	0.435
$\frac{E_2 G_{SS} h^3 b^2}{P^2 l^2 (1-\vartheta_2^2)}$	3.548	3.395	3.376	3.348	3.395	3.282
P_c (N)	262.03	255.82	271.27	272.85	293.24	312.01
G_c (J/m^2)	244.15	222.89	240.00	239.63	277.73	315.04

data of specimen dimension, interface crack length and the load observed in the plateau region of the load-deflection curve. According to the calculated method introduced in Section 2.1, the energy release rates of the sample 3-T(7) and 5-T(7) were calculated by the equation (28) and concluded in Tables 1a and 1b, respectively. The calculated energy release rates of specimens from the same sample were comparable, and the mean value determined for the samples 3-T(7) and 5-T(7) was 259 and 225 J/m^2, respectively.

As analyzed in Section 2.1, the steady-state energy release rate was considered in the four-point bending tests. For sample 3-T(7) the dependence of the energy release rate on the thickness ratio was determined. The dimension and the thickness ratio of each specimen are given in Table 2. By substituting the critical load and the geometry data, the energy release rate is calculated based on the formula (29), and the obtained values are summarized in the Table 2. The mean value of the energy release rate for samples 3-T(7) is 257 J/m^2.

The interface toughness of two FG W/EUROFER multilayers is compared in Fig. 10. The mean toughness of the multilayer with five layers is 225 J/m^2, which is about 13% lower than that of the multilayer with three layers. Nevertheless, the toughness of the same multilayer measured by three- and four-point bending tests, respectively, is more or less similar. Phase angle is a function of the degree of mode mixity on the interface, it varies from 0°(pure Mode I) to 90°(pure Mode II) [29]. Many works have been conducted on investigating the effect of phase angle on interface toughness, in general, the energy release is expected to be lower when the phase angel is smaller [21,30–32]. The phase angle is related to the thickness ratio of the beam and the residual stress [33]. The phase angle is nominally 35°- 60° during four-point bending tests [19]. The larger the thickness ratio, the lower the phase angle [21]. Since the larger thickness ratio represents that the shear load is smaller, and therefore the phase angle is smaller. The thickness ratio h_1/h_2 for sample 5-T(7), sample 3-T(7)_3-Pb and sample 3-T(7)_4-Pb are 0.546, 0.477 and 0.447, respectively. The smaller phase angle of sample 5-T(7) results in the lower energy release rate, which can explain the lower interface toughness of the multilayer with five layers.

The comparison of interface toughness among FG W/EUROFER multilayer and other systems [19–22] is concluded in Fig. 11. As it can be seen, the interface toughness of different systems varies by two orders of magnitude. Besides the SiC/C/SiC performed by three-point bending tests, other systems' interface toughness was measured by performing four-point bending tests. The phase angle introduced by the different measured methods is assumed to be neglected. The fabricating methods are indicated in Fig. 11. The systems (FG W/EUROFER multilayer and B_4C coating on a Ti-6Al-4V substrate) fabricated by VPS show high interface toughness compared to the systems fabricated by sintering and tape casting. The fabricating method plays a key role on the interface quality, and may affect the interface toughness. However, the most prominent difference among them is the typical elastic characteristic of other systems, specifically, the load-deflection curves of the others systems show that the load drops suddenly due to burst of crack and load keeps increasing instead of the plateau form observed in FG W/EUROFER multilayer. Good interface toughness of FG W/EUROFER multilayer is shown by this rough comparison.

4. Conclusion

The energy release rate was evaluated by performing three and four-point bending tests at 550 °C in a vacuum furnace. The load-deflection curve during bending tests provided the critical load of crack propagating along the FG-layer multilayers/substrate interface. Based on beam theory and analytical method, the interface toughness of the investigated samples with 5 and 3 stepwise gradient was 225 and 258 J/m^2, respectively. Hence, the mean toughness of the multilayer with five layers was about 13% lower than that of the multilayer with three layers. Besides the number of layers constituting the FG-layer, thickness ratio of FG W/EUROFER multilayer plays a key role on the difference of toughness. However, the toughness of the same sample measured by three- and four-point bending tests respectively was comparable well. The calculated interface toughness of FG W/EUROFER multilayer is promising, particularly when comparing with those of other systems published in the literature.

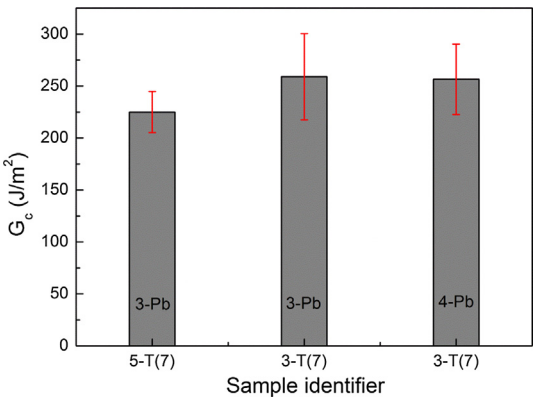

Fig. 10. Comparison on interface toughness of two multilayers.

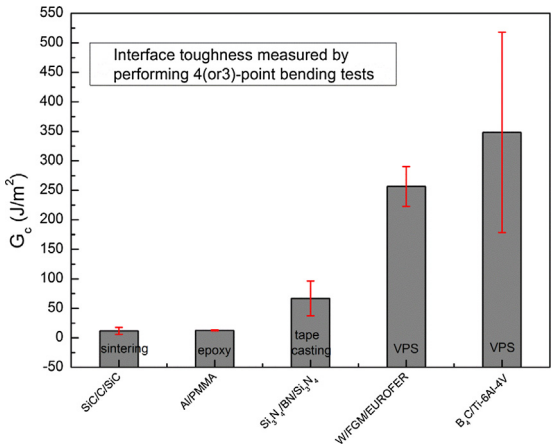

Fig. 11. Comparison on interface toughness among FG W/EUROFER multilayer and other multilayers.

Acknowledgment

This work has been carried out within the framework of the EUROfusion Consortium and has received funding from the Euratom research and training programme 2014–2018 under grant agreement no. 633053. The views and opinions expressed herein do not necessarily reflect those of the European Commission.

References

[1] Boccaccini LV, Aiello G, Aubert J, Bachmann C, Barrett T, Del Nevo A, et al. Objectives and status of EUROfusion DEMO blanket studies. Fusion Eng Des 2016;109–111:1199–206.
[2] Rieth M, Dudarev SL, de Vicente SMG, Aktaa J, Ahlgren T, Autusch S, et al. Recent progress in research on tungsten materials for nuclear fusion applications in Europe. J Nucl Mater 2013;432(1–3):482–500.
[3] Aktaa J, Basuki WW, Weber T, Norajitra P, Krauss W, Konys J. Manufacturing and joining technologies for helium cooled divertors. Fusion Eng Des 2014;89:913–20.
[4] Kohyama A, Hishinuma A, Gelles DS, Klueh RL, Dietz W, Ehrlich K. Low-activation ferritic and martensitic steels for fusion application. J Nucl Mater 1996;233–237:138–47.
[5] Qu DD, Basuki WW, Aktaa J. Numerical assessment of functionally graded tungsten/steel multilayer for first wall applications. Fusion Eng Des 2015;98–99:1389–93.
[6] van der Schaaf B, Tavassoli F, Fazio C, Rigal E, Diegele E, Lindau R, et al. The development of EUROFER reduced activation steel. Fusion Eng Des 2003;69:197–203.
[7] Aktaa J, Lerch M. Near-threshold fatigue crack behaviour in EUROFER 97 at different temperatures. J Nucl Mater 2006;353:101–8.
[8] Weber T, Aktaa J. Numerical assessment of functionally graded tungsten/steel joints for divertor applications. Fusion Eng Des 2011;86:220–6.
[9] Qu DD, Basuki WW, Gibmeier J, Vaßen R, Aktaa J. Development of functionally graded tungsten/EUROFER multilayer for first wall application. Fusion Sci Technol 2015;68:578–81.
[10] Weber T, Stüber M, Ulrich S, Vaßen R, Basuki WW, Lohmiller J, et al. Functionally graded vacuum plasma sprayed and magnetron sputtered tungsten/EUROFER97 interlayers for joints in helium-cooled divertor components. J Nucl Mater 2013;436:29–39.
[11] Thomas G. Advanced materials for plasma facing components in fusion devices, Ph.D thesis. The Queen's College 2009.
[12] Nagasaka T, Kasada R, Kimura A, Ueda Y, Muroga T. Thermophysical properties and microstructure of plasma-sprayed tungsten coating on low activation materials. Fusion Sci Technol 2009;56:1053–7.
[13] Liu Shuo, Tiantang Yu, Bui Tinh Quoc, Xia Shifeng. Size-dependent analysis of homogeneous and functionally graded microplates using IGA and a non-classical Kirchhoff plate theory. Compos Struct 2017;172:34–44.
[14] Liu Shuo, Tiantang Yu, Bui Tinh Quoc. Size effects of functionally graded moderately thick microplates: a novel non-classical simple-FSDT isogeometric analysis. Eur J Mech A/Solids 2017;66:446e458.
[15] Yin Shuohui, Tiantang Yu, Bui Tinh Quoc, Zheng Xuejun, Yi Gao. Rotation-free isogeometric analysis of functionally graded thin plates considering in-plane material inhomogeneity. Thin-Walled Struct 2017;119:385–95.
[16] Bui Tinh Quoc, Van Do Thom, Ton Lan Hoang That, Doan Duc Hong, Tanaka Satoyuki, Pham Dat Tien, et al. On the high temperature mechanical behaviors analysis of heated functionally graded plates using FEM and a new third-order shear deformation plate theory. Compos Part B 2016;92:218–41.
[17] Irwin GR. Onset of fast crack propagation in high strength steel and aluminum alloys. Naval Research Laboratory(NRL) Report 4763; 1956.
[18] Rice JR. A path independent integral and the approximate analysis of strain concentration by notches and cracks. J Appl Mech 1968;35:379–86.
[19] Phillipps AJ, Clegg WJ, Clyne TW. Fracture-behavior of ceramic laminates in bending. 2. Comparison of model predictions with experimental-data. Acta Metallurgica Et Materialia 1993;41(3):819–27.
[20] Zou LH, Huang Y, Chen RF, Wang CA, Park DS. The measurement and characterization of the interfacial toughness of Si3N4/BN composites by a three-point bending test. J Eur Ceram Soc 2003;23(11):1987–96.
[21] Charalambides PG, Lund J, Evans AG, McMeeking RM. A test specimen for determining the fracture resistarim of bimaterial interfaces. J Appl Mech-Trans Asme 1989;56(1):77–82.
[22] Tsui YC, Howard SJ, Clyne TW. The effect of residual stresses on the debonding of coatings – II. An experimental study of a thermally sprayed system. Acta Metall. Mater 1994;42(8):2837–44.
[23] Kolluri M, Hoefnagels JPM, van Dommelen JAW, Geers MGD. A practical approach for the separation of interfacial toughness and structural plasticity in a delamination growth experiment. Int J Fract 2013;183(1):1–18.
[24] Chan KS, Ji H, Wang X, Hudak SJ, Lanning BR. Mechanical properties and interface toughness of FeCo thin films on Ti-6Al-4V. Mater Sci Eng a-Struct Mater Prop Microstruct Process 2006;422(1–2):298–308.
[25] Wang X, Wang C, Atkinson A. Interface fracture toughness in thermal barrier coatings by cross-sectional indentation. Acta Materialia 2012;60(17):6152–63.
[26] Phillipps AJ, Clegg WJ, Clyne TW. Fracture-behavior of ceramic laminates in bending. 1. Modeling of crack-propagation. Acta Metallurgica Et Materialia

1993;41(3):805–17.
[27] Qu DD. Development of functionally graded tungsten/EUROFER multilayers, Ph.D thesis. Karlsruhe Institute of Technology (KIT); 2016.
[28] Aktaa J, Kecskés S, Pereslavtsev P, Fischer U, Boccaccini LV. Non-linear failure analysis of HCPB blanket for DEMO taking intoaccount high dose irradiation. Fusion Eng Des 2014;89:1664–8.
[29] Tadepalli R, Turner KT, Thompson CV. Mixed-mode interface toughness of wafer-level Cu–Cu bonds using asymmetric chevron test. J Mech Phys Solids 2008;56:707–18.
[30] Charalambides PG, Evans AG. Debonding properties of residually stressed brittle-matrix composites. J Am Ceram Soc 1989;72(5):746–53.
[31] Bose K, Mataga PA, Castaneda PP. Stable crack growth along a brittle:ductile interface-II. Small scale yielding solutions and interfacial toughness predictions. Int J Solids Struct 1999;36:1–34.
[32] Aoki S, Ishii N. An interface crack under mixed-mode loading. Model Simul Mater Sci Eng 1994;2:473–82.
[33] Howard SJ, Tsui YC, Clyne TW. The effect of residual stresses on the debonding of coatings – I. A model for delamination at a bimaterial interface. Acta Metall Mater 1994;42(8):2823–36.